



**HAL**  
open science

# Global sensitivity analysis of the dynamics of a distributed hydrological model at the catchment scale

Katarina Radišić, Emilie Rouzies, Claire Lauvernet, Arthur Vidard

## ► To cite this version:

Katarina Radišić, Emilie Rouzies, Claire Lauvernet, Arthur Vidard. Global sensitivity analysis of the dynamics of a distributed hydrological model at the catchment scale. *Socio-Environmental Systems Modelling*, In press, pp.1-20. hal-03884443v1

**HAL Id: hal-03884443**

**<https://hal.inrae.fr/hal-03884443v1>**

Submitted on 7 Dec 2022 (v1), last revised 26 Oct 2023 (v2)

**HAL** is a multi-disciplinary open access archive for the deposit and dissemination of scientific research documents, whether they are published or not. The documents may come from teaching and research institutions in France or abroad, or from public or private research centers.

L'archive ouverte pluridisciplinaire **HAL**, est destinée au dépôt et à la diffusion de documents scientifiques de niveau recherche, publiés ou non, émanant des établissements d'enseignement et de recherche français ou étrangers, des laboratoires publics ou privés.



Distributed under a Creative Commons Attribution 4.0 International License

# Global sensitivity analysis of the dynamics of a distributed hydrological model at the catchment scale

Radišić Katarina<sup>1,2</sup>, Rouzies Emilie<sup>1</sup>, Lauvernet Claire<sup>1</sup>, and Vidard Arthur<sup>2</sup>

<sup>1</sup>INRAE, RiverLy, 69625, Villeurbanne, France

<sup>2</sup>Univ. Grenoble Alpes, Inria, CNRS, Grenoble INP, LJK, 38000 Grenoble, France

---

---

## Abstract

The PESHMELBA model simulates water and pesticide transfers at the catchment scale. Its objective is to help the process of decision making in the common management of long-term water quality. Performing the global sensitivity analysis (GSA) of this type of model is necessary to trace the output uncertainties to the input parameters. The goal of the present work is to perform a GSA, while considering the spatio-temporal nature and the high dimensionality of the model. The output considered is the surface moisture simulated over a two month period on a catchment of assorted mesh elements (*plots*). The GSA is performed on the dynamical outputs, rewritten through their functional principal components. Sobol' indices are then estimated through polynomial chaos expansion on each principal component. The analysis differs between the two types of behaviour observed in the surface moisture outputs. The hydrodynamic properties of the surface soil have a dominant influence on the average surface moisture. Nonetheless, the parameters describing deeper soil layers influence the output dynamics of those plots where the surface moisture is saturated. We obtain Sobol' indices with high precision while using a limited number of model estimations and considering the models spatio-temporal nature. The physical interpretation of the GSA confirms and augments our knowledge on the model.

## Keywords

Global sensitivity analysis; hydrology; functional principal components; polynomial chaos expansion; distributed model

---

---

## 1 Introduction

Pesticide use is a major issue in sustainable agriculture and water quality. Therefore, it is important to have the knowledge and the tools to best estimate the risks associated with their use and propose appropriate corrective actions. The PESHMELBA model (PESticides et Hydrologie, Modélisation à l'EcheLle du BAssin versant, Pesticides and Hydrology: modeling at the catchment scale, Rouzies et al. (2019)) simulates processes involved in water and pesticide transfers at the catchment scale, in order to compare different scenarios of landscape management and their impact on water quality.

An important step in the journey to PESHMELBA's operational use is to perform a thorough study on the model uncertainties. Global sensitivity analysis is useful in this case, as it can trace the output uncertainties back to its input parameters. It can also verify the model consistency with respect to the physical processes and enhance the understanding of the modeled behavior. However, PESHMELBA outputs are both space and time dependent and the application of global sensitivity analysis to spatio-temporal environmental models can be challenging and dependent on the particular case studied.

Traditionally, sensitivity analysis methods based on Sobol' (2001) were developed for scalar outputs (Saltelli et al., 2008), but many extensions of sensitivity indices to multivariate (spatial or temporal) output have been introduced. Some are variance-based (Gamboa et al. (2014), Lamboni et al. (2011), see also Xiao & Li (2016), Xu et al. (2019), Roux et al. (2021)), while others use different dependence measures such as the HSIC (Da Veiga (2015), Marrel et al. (2015)) or random forests (Antoniadis et al. (2021)).

The extensions were used in various modeling areas. For instance, a sensitivity analysis on the spatialized maximum water depth of a coastal flooding risk model in Perrin et al. (2021). Both a temporal and a spatial sensitivity analysis of a model describing nitrogen transfers in Ferrer Savall et al. (2019). Comparison between various sensitivity indices on a spatio-temporal radionuclide atmospheric dispersion model in De Lozzo & Marrel (2017).

A sensitivity analysis was also performed for spatially distributed PESHMELBA outputs in Rouzies et al. (2021) by calculating site specific sensitivity indices, then aggregating them to blocks via the definition provided in Gamboa et al. (2014). However, the sensitivity of the dynamics of PESHMELBA outputs was not a goal of this study.

As the previous examples show, there is no universal methodology for performing a sensitivity analysis on spatio-temporal models. Both the choice of the sensitivity index and its estimator can be guided by various model properties such as the space resolution, time resolution or the nature of the input parameters (scalar or multivariate). Other important aspects are the number of input parameters and the cost of a model run, since the number of model runs needed for sensitivity analysis increases with the number of input parameters.

Metamodels, in particular polynomial chaos expansion (PCE), can be used for sensitivity index calculation at a reasonable cost and high efficiency. They are especially useful when the model studied is computationally expensive or has a large input space. Indeed, building a PCE via Least Angle Regression (Blatman & Sudret, 2011) needs a significantly lower number of model simulations than other Monte Carlo based methods. Furthermore, once the metamodel is built, the sensitivity index calculation is analytical (Sudret, 2008). Applications of PCE for Sobol index calculation can be found in (Fajraoui et al., 2011) or in (Rouzies et al., 2021).

The present work is an application of a combination of existing global sensitivity analysis methods, with the goal of obtaining sensitivity indices while considering the spatio-temporal nature of the highly dimensional water and pesticide transfer model PESHMELBA. The outputs considered are the surface moisture outputs simulated over a two month period on a catchment of assorted mesh elements (*plots*). In this study, the plots are observed one at a time. The sensitivity analysis is performed on their temporal outputs, which are rewritten through their principal components. Then, Sobol' indices are estimated through polynomial chaos expansion on each principal component.

The article is organized as follows. We present in Section 2 the methodology, a brief description of Sobol' indices and their estimation via polynomial chaos expansion, then the functional principal component decomposition and two generalizations of sensitivity indices when the outputs are multidimensional. Section 3 presents the case study. The model PESHMELBA is introduced and the meaning of its input parameters explained. The results are presented in Section 4 in the following order. First, the resulting functional principal components are interpreted for each plot, then each PCE is validated, the Sobol' indices obtained are reported and commented by making a connection with the physics of the model. Finally the Sobol' indices are aggregated temporally and spatially to the catchment scale.

## 2 Methodology

Let  $\mathcal{M} : \mathbb{R}^K \rightarrow \mathbb{R}$  be a model with  $K$  mutually independent scalar inputs  $X_1, \dots, X_K$  and a scalar output  $Y$ .

$$Y = \mathcal{M}(X_1, \dots, X_K) = \mathcal{M}(\mathbf{X})$$

### 2.1 Sobol' Indices

The Sobol' indices are a widely accepted way of quantifying the sensitivity of the model output on the input parameters. The Sobol' approach is variational; it studies the impacts of input parameters on the output variance.

Let  $D$  be the variance of the model output  $Y$ :

$$D = \text{Var}(Y).$$

Let  $D_i$  be the variance of the expectation of the output conditioned on input parameter  $X_i$ :

$$D_i = \text{Var}(\mathbb{E}[Y|X_i]).$$

Then, the first order Sobol' indices of the input parameter  $X_i$  are defined as the ratio between the conditional variance and the total variance of the output (Sobol', 2001):

$$S_i = D_i/D.$$

Let  $D_{i_1, \dots, i_s}$  be the variance of the expectation of the output conditioned on the set of input parameters  $\{X_{i_1}, \dots, X_{i_s}\}$  minus the variance of the expectation of the output conditioned on all other subsets of the given set:

$$D_{i_1, \dots, i_s} = \text{Var}(\mathbb{E}[Y|X_{i_1}, \dots, X_{i_s}]) - \sum_{\mathcal{I}_s} D_{i_1, \dots, i_k},$$

$$\mathcal{I}_s = \{\{i_1, \dots, i_k\} : \{i_1, \dots, i_k\} \subsetneq \{i_1, \dots, i_s\}\}.$$

Similarly, the Sobol index of the set of input parameters  $X_{i_1}, \dots, X_{i_s}$  is defined as the ratio between the conditional variance of the output to those parameters minus the variances of the output conditioned to any other subset of the concerned input parameters, and the total variance of the output:

$$S_{i_1, \dots, i_s} = D_{i_1, \dots, i_s}/D.$$

The total Sobol' index of input parameter  $X_i$  is defined as the sum of all Sobol' indices of those sets which contain it.

$$S_{T_i} = \sum_{\mathcal{I}_i} D_{i_1, \dots, i_s}/D,$$

$$\mathcal{I}_i = \{\{i_1, \dots, i_s\} : \exists k, 1 \leq k \leq s, i_k = i\}.$$

As all Sobol indices of first order and Sobol indices of higher orders sum up to 1, an alternative definition for the total Sobol index is:

$$S_{T_i} = 1 - S_{\sim i},$$

where  $S_{\sim i}$  is the sum of all Sobol indices  $S_{i_1, \dots, i_s}$  that do not include index  $i$ .

Sobol' indices have some nice properties such as explaining explicitly the influence of a parameter on its own (first order Sobol' indices) or in interaction with other parameters (total Sobol' indices). However, estimating them is not always an easy task, especially when it comes to large models with many input parameters and computationally expensive simulations.

## 2.2 Polynomial chaos expansion and the link with Sobol' indices

Except for simple analytical models, Sobol' indices are typically calculated via stochastic methods (Saltelli et al., 2008). Obtaining precise Sobol' indices via these methods requires an efficient exploration of the input parameters' space. One of the main challenges is dealing with large input spaces. Many points are needed to explore a highly dimensional space (curse of dimensionality). As each point is evaluated via the original model, this task becomes difficult when the original model is computationally expensive. In this work, polynomial chaos expansions (PCE) are used to reduce the cardinality of the experimental design (Sudret, 2008).

The model output can be rewritten via its polynomial chaos expansion decomposition as:

$$Y = \sum_{\alpha \in \mathbb{N}^K} y_\alpha \Psi_\alpha(\mathbf{X}) = \mathcal{M}(\mathbf{X}) \quad (1)$$

where  $K$  is the number of input parameters,  $\{\Psi_\alpha\}_{\alpha \in \mathbb{N}^K}$  is a basis of multivariate orthonormal polynomials, constructed according to the marginal probability density functions  $f_{X_i}$  of the input parameters,  $\alpha \in \mathbb{N}^K$  are multi-indices, i.e.  $\alpha = (\alpha_1, \alpha_2, \dots, \alpha_K)$  where each  $\alpha_i$  corresponds to the partial degree with which the  $i$ th entry parameter  $X_i$  is represented in the basis component  $\Psi_\alpha$  and  $y_\alpha$  coefficients ( $y_\alpha$  are the coordinates of the output  $Y$  in the new vectorial space defined by the basis  $\{\Psi_\alpha\}_{\alpha \in \mathbb{N}^K}$ ).

Once the model  $\mathcal{M}$  is rewritten via its polynomial chaos expansion, the Sobol' indices are obtained analytically from the coefficients  $y_\alpha$ , (Sudret, 2008).

Indeed, by adding the squares of all coefficients  $y_\alpha$  whose multi-index's  $\alpha$  only non-null index is the  $i$ th index  $\alpha_i \neq 0$ , and dividing it by the total variance of the PCE metamodel  $D$ , we obtain the Sobol' index of first order of the input parameter  $X_i$ :

$$S_i = \sum_{\alpha \in \mathcal{I}_i} y_\alpha^2 / D,$$

$$\mathcal{I}_i = \{ \alpha \in \mathbb{N}^K : \alpha_i > 0, \alpha_{j \neq i} = 0 \},$$

$$D = \text{Var} \left[ \sum_{\alpha \in \mathcal{I}} y_\alpha \Psi_\alpha(\mathbf{X}) \right] = \sum_{\substack{\alpha \in \mathcal{I} \\ \alpha \neq 0}} y_\alpha^2.$$

Similarly, by adding the squares of coefficients  $y_\alpha$  whose multi-index  $\alpha$  satisfies certain properties, the Sobol' indices of a set of input parameters and the total Sobol' indices are also obtained analytically:

$$S_{i_1, \dots, i_s} = \sum_{\alpha \in \mathcal{I}_{i_1, \dots, i_s}} y_\alpha^2 / D,$$

$$\mathcal{I}_{i_1, \dots, i_s} = \{ \alpha \in \mathbb{N}^K : k \in \{i_1, \dots, i_s\} \Leftrightarrow \alpha_k \neq 0 \},$$

$$S_i^T = \sum_{\alpha \in \mathcal{I}_i^T} y_\alpha^2 / D,$$

$$\mathcal{I}_i^T = \{ \alpha \in \mathbb{N}^K : \alpha_i > 0 \}.$$

Thus, the difficulty and the computational cost of calculating the Sobol' indices for the original model  $\mathcal{M}$  can be replaced with the difficulty and the computational cost of finding a polynomial chaos expansion  $\mathcal{M}_{PCE}$  which approximates the behavior of the original model "well enough".

Section 2.3 explains how to estimate  $\mathcal{M}_{PCE}$ , how to limit the cardinality of the experimental design and lastly, how to evaluate if  $\mathcal{M}_{PCE}$  is true to the original model.

### 2.3 Estimation of a polynomial chaos expansion

Let the model  $\mathcal{M} : \mathbb{R}^K \rightarrow \mathbb{R}$  from the beginning of Section 2 be the original model for which we want to build a PCE. Let  $f_{X_i}$  be the marginal probability density function of input parameter  $X_i$ . The goal is to estimate a  $\mathcal{M}_{PCE}$  polynomial chaos expansion of the original model by using a limited number  $N_{training}$  of original model evaluations:

$$\mathcal{M}(\mathbf{X}) = Y \approx \sum_{\alpha \in \mathcal{A}_{p,q}^K} y_\alpha \Psi_\alpha(\mathbf{X}) = \mathcal{M}_{PCE}(\mathbf{X}).$$

The first step in PCE approximation is to choose the truncation scheme for  $\alpha$ , denoted by  $\mathcal{A}_{p,q}^K$ . Popular truncation schemes limit the maximum degree with which the input parameters  $X_i$  are represented in the basis. This is done by setting an upper limit  $p$  such that  $\alpha_i < p$  for every  $i$ . The heuristics behind this truncation being that most of the influence of the input parameters is captured in low orders of the multivariate polynomials (Le Gratiet et al., 2015). For a PCE metamodel with  $K$  input parameters and  $p$  the maximum degree of the basis polynomial, the cardinality of the basis  $\text{card}(\mathcal{A}_p^K) = \binom{K+p}{p}$  increases exponentially with respect to the number of input parameters  $K$ .

To further reduce the basis cardinality, the degree of interaction between the input parameters can be limited. This is done by introducing  $q \in (0, 1)$  and imposing the  $q$ -norm of  $\alpha$  to be limited by  $p$ , i.e.  $\|\alpha\|_q = (\sum_{i=1}^K \alpha_i^q)^{1/q} < p$ . Limiting the interactions between input parameters is justified with the sparsity of effects (Le Gratiet et al., 2015). This type of truncation shows a drastic decrease in cardinality of  $\mathcal{A}_{p,q}^K$  for a fixed  $p$ .

Once the truncation scheme is chosen, the creation of the basis  $\{\Psi_\alpha\}_{\alpha \in \mathcal{A}_{p,q}^K}$  is straightforward, as it is characterized by the marginal probability density functions  $f_{X_i}$ . The estimation of the PCE reduces to the estimation

of the coefficients  $y_\alpha$ . To estimate the PCE coefficients  $y_\alpha$  comes down to a linear regression on a training sample of pairs of inputs and model outputs  $\{(\mathbf{x}_1, \mathcal{M}(\mathbf{x}_1)), (\mathbf{x}_2, \mathcal{M}(\mathbf{x}_2)), \dots, (\mathbf{x}_{N_{\text{training}}}, \mathcal{M}(\mathbf{x}_{N_{\text{training}}}))\}$ .

The number of coefficients  $y_\alpha$  to estimate is equal to  $\text{card}(\mathcal{A}_{p,q}^K)$ . In order for the linear regression to be successful,  $N_{\text{training}}$  should be at least as big as the number of coefficients to estimate. However, the lack of the hypothesis  $N_{\text{training}} \gg \text{card}(\mathcal{A}_{p,q}^K)$  can further be tackled via least angle regression (LARS, Blatman & Sudret (2011)).

Whether the approximated metamodel  $\mathcal{M}_{PCE}$  is a good replacement of the original model  $\mathcal{M}$  is evaluated via the coefficient of determination  $R^2$  on a test set  $\{(\mathbf{x}_1, \mathcal{M}(\mathbf{x}_1)), (\mathbf{x}_2, \mathcal{M}(\mathbf{x}_2)), \dots, (\mathbf{x}_{N_{\text{test}}}, \mathcal{M}(\mathbf{x}_{N_{\text{test}}}))\}$ . These estimations are not used for the calculation of the PCE metamodel coefficients  $y_\alpha$ . The coefficient of determination  $R^2$  measures the quality of the prediction of a linear regression:

$$R^2 = 1 - \frac{\sum_{n=1}^{N_{\text{test}}} (\mathcal{M}(\mathbf{x}_n) - \mathcal{M}_{PCE}(\mathbf{x}_n))^2}{\sum_{n=1}^{N_{\text{test}}} (\mathcal{M}(\mathbf{x}_n) - \bar{\mathcal{M}})^2}, \quad (2)$$

where  $\mathcal{M}(\mathbf{x}_n)$  is the evaluation of the original model for input parameters set to values  $\mathbf{x}_n$ ,  $\mathcal{M}_{PCE}(\mathbf{x}_n)$  is the evaluation of the PCE metamodel for input parameters set to values  $\mathbf{x}_n$ , and  $\bar{\mathcal{M}}$  is the mean of all original model evaluations,  $\bar{\mathcal{M}} = \sum_{n=1}^{N_{\text{test}}} \mathcal{M}(\mathbf{x}_n)$ . The closer the  $R^2$  is to 1, the better is  $\mathcal{M}_{PCE}$  in approximating  $\mathcal{M}$ .

The estimated Sobol indices are calculated analytically from the coefficients of  $\mathcal{M}_{PCE}$ :

$$\hat{S}_i = \sum_{\alpha \in \mathcal{I}_i^*} y_\alpha^2 / D, \quad (3)$$

$$\mathcal{I}_i^* = \{\alpha \in \mathcal{A}_{p,q}^K : \alpha_i > 0, \alpha_{j \neq i} = 0\}.$$

The precision of the estimated Sobol' indices can be quantified by creating multiple resamples with replacement of the original experimental design and calculating the Sobol' indices from each resample. The confidence intervals obtained on the Sobol' indices are called bootstrap confidence intervals (Dubreuil et al., 2014).

## 2.4 Sensitivity analysis when model outputs are multidimensional

In previous sections we have seen the definitions of Sobol' indices and their estimation for a model with  $K$  independent scalar inputs and a scalar output. However, it often happens that the model whose sensitivity we wish to study produces outputs over a given time period.

Let  $\mathcal{M}$  be a model with  $K$  independent scalar inputs and a dynamic output over a time interval  $\mathcal{T}$ :

$$Y(t) = \mathcal{M}(\mathbf{X}, t), \quad t \in \mathcal{T}. \quad (4)$$

Set  $\mu(t) = \mathbb{E}[Y(t)]$  and assume the output random function to be square integrable:  $\int_0^T \mathbb{E}(Y^2(t)) dt < \infty$ . We can rewrite the output random function via its principal component (PC) expansion:

$$Y(t) = \mu(t) + \sum_j H_j \mathbf{v}_j(t), \quad (5)$$

where  $\mathbf{v}_j(t)$  is the  $j$ th functional principal component (also called harmonic or mode), and  $H_j \in \mathbb{R}$  is the  $j$ th functional principal component score (Ramsay & Silverman, 2005).

By decomposing the random variable  $Y(t)$  into its principal components (Eq. 5), the variability of  $Y(t)$  is rewritten in terms of the variabilities of the principal components  $H_j$ . The variability of the  $j$ th PC score  $H_j$  is denoted with  $\lambda_j$ . The  $\lambda_j$  are decreasing with respect to  $j$  by construction.

By truncating the series to the first  $J$  PCs we obtain an approximation of the output:

$$Y(t) \approx \mu(t) + \sum_{j=1}^J H_j \mathbf{v}_j(t), \quad (6)$$

which accounts for  $\sum_{j=1}^J \lambda_j / \sum_j \lambda_j$  of the total variance in the output  $Y(t)$ . Oftentimes,  $J$  is chosen by first setting the percentage of total inertia observed in the output that we wish to account for. Then, the number of PCs  $J$  that should be kept is deduced. Another choice is to directly set the number of PCs that will be studied. As the scores  $H_j$  are scalar quantities, all theory developed in previous sections for models with scalar outputs can be applied. Thus, Sobol' indices can be obtained for one PC at a time. Furthermore, in order to have a synthetic sensitivity index for dynamic outputs, rather than sensitivity indices on each PC, the following definition of a generalized sensitivity index is proposed in Lamboni et al. (2011):

$$GSI_w = \frac{\sum_j \lambda_j SI_{w,j}}{\sum_j \lambda_j}, \quad (7)$$

where  $w$  is the group of the input parameters,  $SI_{w,j}$  is the sensitivity index of inputs  $w$  on the  $j^{th}$  PC.

Gamboa et al. (2014) propose another way of aggregating sensitivity indices calculated on individual outputs of a model with multidimensional outputs :

$$ASI_w = \frac{\sum_{m=1}^M \text{Var}(Y^{(m)}) SI_{w,m}}{\sum_{m=1}^M \text{Var}(Y^{(m)})}, \quad (8)$$

where  $Y^{(m)}$  is the  $m^{th}$  component of the  $M$ -dimensional output and  $SI_{w,m}$  is the sensitivity index of the set of input parameters  $w$  on the  $m^{th}$  component of the output.

The two definitions coincide when the total variability of the output can be described with a finite number of principal components (De Lozzo & Marrel, 2017).

### 3 Case study

The PESHMELBA model simulates water and pesticide transfers at the catchment scale of the Morcille river in the Beaujolais wine region. The heterogeneity of the catchment's soil and vegetation types is represented by dividing the catchment in different *plots*. In the studied case, the virtual catchment is divided in  $M = 14$  plots, each belonging to one of three soil units (SU): SU1 (sandy soil), SU2 (sandy soil on clay) or SU3 (heterogeneous sandy soils), illustrated in Figure 1. The virtual catchment is presented with more details in Rouzies et al. (2021).

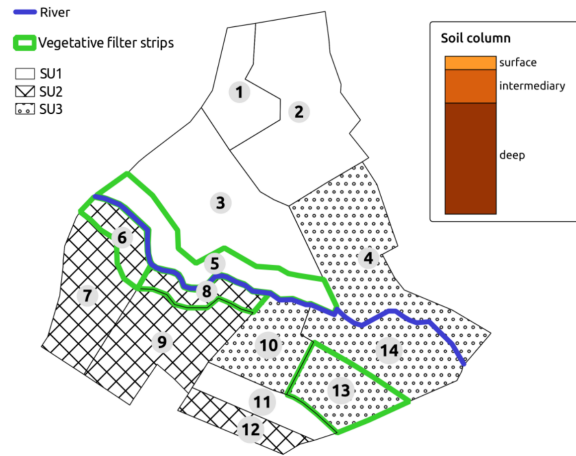


**Figure 1:** The decomposition of the virtual catchment in 14 plots numbered with  $m \in \{1, \dots, 14\}$ . Each plot belongs to one of the three possible soil units, depicted by different fillings and has one of two possible vegetation types, depicted by the plot's borders (vegetative filter strips have a bold green border, whereas vineyard plots have fine black borders). The separation of the soil column under each plot into three soil horizons (surface, intermediary and deep) is illustrated in the upper right corner. The depths of the soil horizons varies from one SU to another (Image from Rouzies et al. (2021)).

PESHMELBA is a three-dimensional model, where the heterogeneity of the soil layers along the vertical axis is also taken into account. Indeed, the soil column under each plot is decomposed in three layers (*soil horizons*),

as in Figure 1. The depth of the soil horizons and their soil properties vary from one SU to another. The soil horizons are considered internally homogeneous when it comes to soil hydrodynamical properties.

PESHMELBA has a modular structure, simulating the physical processes of each soil compartment, then coupling them via the OpenPALM coupler (Buis et al., 2006). The coupling allows for water and pesticide transfers to occur via three types of transfer pathways: infiltration (Richards' equation solved by Ross (2003)), surface runoff (kinematic wave equation) and lateral exchanges (Darcy law). Surface runoff occurs on the surface of the catchment, whereas lateral exchanges refer to subsurface transfers occurring in saturated zones. One may refer to Rouzies et al. (2019) for more details.

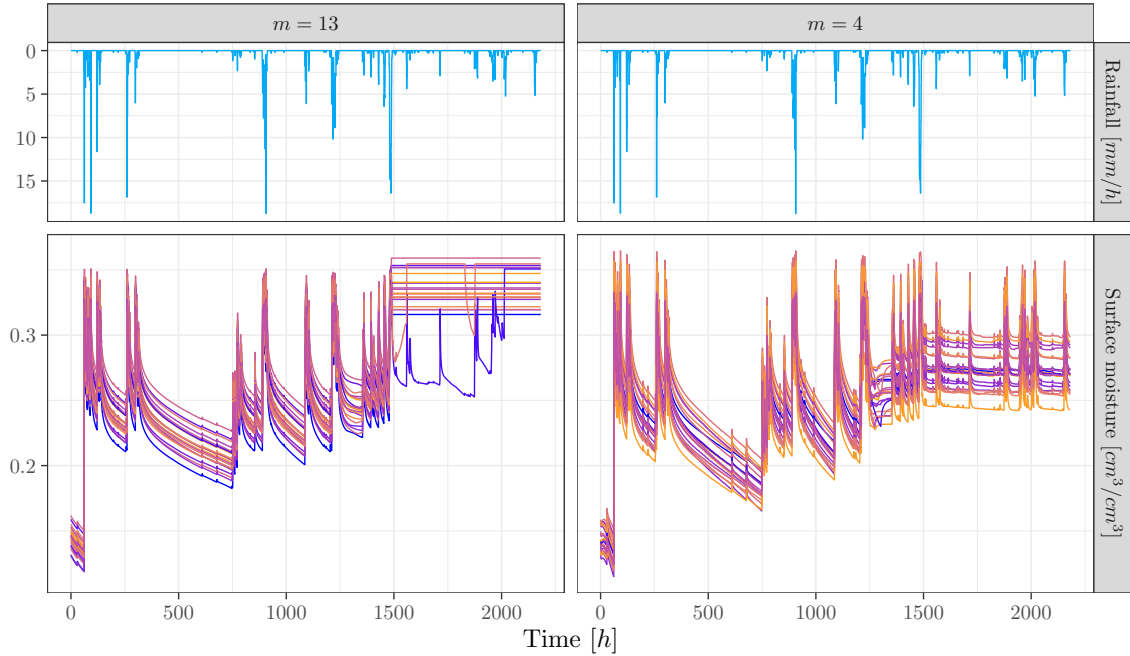


**Figure 2:** Top row: rainfall time series. The same rainfall time series was applied across all simulations and all plots. Bottom row: surface moisture outputs of 20 PESHMELBA model simulations with different input parameter values. Different simulations are represented with various shades between orange and purple following no particular order. Outputs are reported for two plots,  $m = 13$  on the left and  $m = 4$  on the right.

Representing the physical properties of each soil horizon of the catchment results in a large number of input parameters. Indeed, in the case studied the PESHMELBA model has 145 input parameters. The number of inputs of interest for the sensitivity analysis was reduced to 52 via a previous screening step performed with the elementary effects method (Morris, 1991) not shown here. The marginal probability distributions of the remaining  $K = 52$  input parameters are listed in Table 3.

A soil unit is always made out of the same soil horizons; plots  $\{1, 2, 3, 11\} \in SU1$  are all made of the same soil horizons, and the same goes for  $\{4, 10, 14\} \in SU2$  and  $\{7, 9, 12\} \in SU3$ . The previously listed plots correspond to vineyard plots, while the remaining plots  $\{5, 6, 8, 13\}$  correspond to vegetative filter strips. A vineyard plot and a vegetative filter strip belonging to the same soil type differ in their surface soil horizon. Indeed, the surface horizon of the vegetative filter strip has a higher infiltration capacity and adapted hydrodynamical properties, while the intermediary and deep horizon maintain the same properties as the vineyard plot.

As an example, the plot 8 and the plot 9 are both of soil type SU2, but 8 is a vegetative filter strip, whereas 9 is a vineyard plot. The physical properties of the deep and intermediary horizons of both plots are described by the input parameters with the suffix *interm\_soil2* and *deep\_soil2*, respectively. The physical properties of the surface soil horizon of plot 9 are described with the input parameters having the suffix *surf\_soil2*; whereas the input parameters describing the properties of surface soil horizon of plot 8 are named with the suffix *surf\_soil2(VFZ)*.

The output studied in this work is the surface moisture series simulated at 2712 consecutive time steps, corresponding to roughly 2500 hours or three months. The output consists in  $M = 14$  time series, one for each plot. An illustration of these outputs is provided in Figure 2 for two plots,  $m = 13$  and  $m = 4$ . It can be seen that the dynamics of the outputs is closely driven by rainfall events. Indeed, the peaks in surface moisture are reached right after the rain events.

Furthermore, we observe that most outputs of plot  $m = 13$  result in the saturation of the surface moisture starting from around time  $t = 1500h$ . On the other hand, the surface moisture of plot  $m = 4$  does not reach its full saturation during the simulation time. Two types of behaviors are observed in the surface moisture time series. Plots  $\{2, 3, 7, 9, 13\} = \mathcal{G}_{sat}$  show a saturation in water retention after  $t = 1500h$  of the simulated period for most of the simulated outputs, on Figure 2 for  $m = 13$ . On the other hand, the surface moisture of plots  $\{1, 4, 5, 6, 8, 10, 11, 12, 14\} \notin \mathcal{G}_{sat}$  do not saturate during the simulated period, on Figure 2 for  $m = 4$ .

The rainfall time series is considered to be the same across all simulations and plots; its value is fixed to a time series measured in a typical winter scenario dimensioned on the catchment. Thus, the sensitivity of the outputs with respect to the rain is not tackled in this study. Here, all input parameters are scalar and independent. Furthermore, as the time steps are close, we consider the time to be continuous. The model can be written as:

$$\begin{bmatrix} Y^{(1)}(t) \\ Y^{(2)}(t) \\ \vdots \\ Y^{(M)}(t) \end{bmatrix} = \mathcal{M}(\mathbf{X}, t), \quad t \in \mathcal{T}, \quad (9)$$

with  $M = 14$  the number of plots,  $\mathbf{X} \in \mathbb{R}^K$  the  $K = 52$  input parameters and  $\mathcal{T}$  the time period in consideration.

## 4 Results and discussion

A space-filling experimental design of  $N_{training} = 3000$  points is created over the  $K = 52$  dimensional input space. The space-filling design used is a latin hypercube, optimized with the maximin criteria. The PESHMELBA model is evaluated in these points and this sample is used to calculate the first two principal components for each plot. Section 4.1 shows the principal component analysis and interprets the principal components. The same sample is used to build a metamodel for the first two principal components of each plot. A second latin hypercube sample of  $N_{test} = 1000$  points is generated on the  $K = 52$  dimensional input space for the evaluation of the metamodels. Section 4.2 studies the quality of the metamodels built. The Sobol' indices for the principal components of the dynamic outputs are found analytically from the metamodel coefficients following Section 2.2 and Section 2.3. In Section 4.3 the Sobol' indices are reported and their physical meaning is commented.

### 4.1 Functional principal components

One plot  $m \in \{1, \dots, 14\}$  is fixed and its  $N_{training} = 3000$  temporal outputs  $Y^{(m)}$  are observed. The outputs represent the surface moisture time series of the plot  $m$  over the period  $\mathcal{T}$ . The outputs are supposed continuous. For a fixed plot  $m$ , the model can thus be written as in Eq. 4. Then, a functional principal component basis is found for the plot  $m$ . The basis is truncated to the first two components:

$$Y^{(m)}(t) \approx \mu^{(m)}(t) + H_1^{(m)} \mathbf{v}_1^{(m)}(t) + H_2^{(m)} \mathbf{v}_2^{(m)}(t).$$

The part of the total variance explained with the first two principal components PC1 and PC2 is listed in Table 1 per plot. Two groups of plots with similar behavior are identified. A first group, with more than 90% of the total output variability explained with PC1 and less than 2% with PC2, and a second group, where the variability explained by PC1 is a bit lower, but still superior to 80%, whereas PC2 accounts for more than 7%.

Interestingly, the two groups coincide with  $\{2, 3, 7, 9, 13\} \in \mathcal{G}_{sat}$  and  $\{1, 4, 5, 6, 8, 10, 11, 12, 14\} \notin \mathcal{G}_{sat}$ , the groups identified in Section 3 by a study of their outputs; the plots in  $\mathcal{G}_{sat}$  showing a saturation of the water content in their surface.

**Table 1:** Percentage of the total variability observed in the output of plot  $m$  captured for with the  $j$ th PC, i.e.  $\lambda_j^{(m)} / \sum_j \lambda_j^{(m)}$ .

$m$	1	2	3	4	5	6	7	8	9	10	11	12	13	14
$PC1$	0.99	0.82	0.89	0.96	0.99	0.95	0.85	0.99	0.81	0.96	0.99	0.94	0.83	0.97
$PC2$	<0.01	0.16	0.08	0.02	<0.01	0.02	0.07	<0.01	0.10	0.02	<0.01	0.03	0.13	0.02
$PC1 + PC2$	0.99	0.98	0.97	0.98	0.99	0.97	0.92	0.99	0.91	0.98	0.99	0.97	0.96	0.99

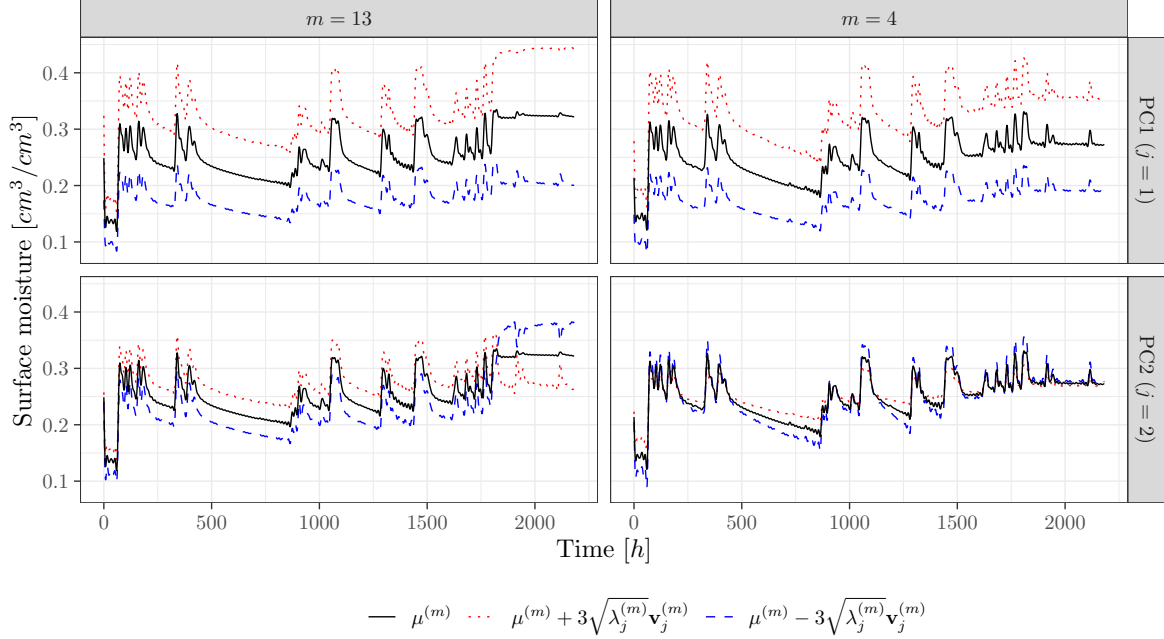


**Figure 3:** Perturbations on the first two PCs of plots  $m = 4 \notin \mathcal{G}_{sat}$  on the left column and  $m = 13 \in \mathcal{G}_{sat}$  on the right column. The top row shows the perturbations in the direction of PC1, the bottom row shows the perturbations on PC2. The mean of the sample outputs is presented with a solid black line. The red dotted line and the blue dashed line represent the output that is three standard deviations away from the mean in the direction of the corresponding PC.

The presence of the two groups is not only limited to the percentages of variances explained by the first two PCs. The plots belonging to the same group also yield the same interpretation for their PCs. The perturbations on the first two PCs of the plots  $m = 13 \in \mathcal{G}_{sat}$  and  $m = 4 \notin \mathcal{G}_{sat}$  can be seen in Figure 3. Only one plot is chosen from each group as the interpretations of the PCs are the same for all plots inside the same group.

From the top row in Figure 3, we can interpret the first principal component (PC1) as the vertical shift of the output time series. Thus, the outputs having a low score on the PC1 have a low average surface moisture on the whole simulation period, similar to the blue dashed line; on the other hand the outputs scoring highly on the PC1 have a high surface moisture, similar to the red dotted line. The interpretation of the PC1 is the same for both  $m = 13 \in \mathcal{G}_{sat}$  and  $m = 4 \notin \mathcal{G}_{sat}$ .

On the contrary, the second principal component (PC2) explains different behaviors in the two groups. Indeed, the PC2 of plot  $m = 4 \notin \mathcal{G}_{sat}$  is interpreted as the amplitude of the outputs (infiltration rate), whereas the PC2 of plot  $m = 13 \in \mathcal{G}_{sat}$  is interpreted as the contrast between the surface moisture during the plateau and outside the plateau: outputs scoring highly on PC2 do not display significant change in moisture during the plateau and outside the plateau, whereas the outputs with low scores on PC2 have a surface moisture much higher during the plateau than outside of the plateau.

## 4.2 Polynomial chaos expansion

For each plot  $m \in \{1, \dots, 14\}$ , a PCE is built independently for the first principal component (PC1). A PCE is also built for the second principal components (PC2) of plots  $m \in \{1, \dots, 14\} \setminus \{1, 8, 9, 11\}$ . Indeed, the plots  $\{1, 8, 9, 11\}$  are excluded as their PC1 alone already accounts for more than 99% of the total variability in the training sample, thus their PC2 accounts for less than 1% of the total output variance (Table 1).

To sum up, the following input-output relations are estimated through polynomial chaos expansion :

$$\begin{aligned} H_1^{(m)} &= \mathcal{M}_1^{(m)}(\mathbf{X}) \quad \forall m \in \{1, \dots, 14\} \\ H_2^{(m)} &= \mathcal{M}_2^{(m)}(\mathbf{X}) \quad \forall m \in \{1, \dots, 14\} \setminus \{1, 8, 9, 11\} \end{aligned}$$

Where  $H_1^{(m)}$  (resp.  $H_2^{(m)}$ ) are the scores obtained on PC1 (resp. PC2) of plot  $m$  and  $\mathbf{X}$  is the vector of the  $K = 52$  independent input parameters with marginal distributions reported in Table 3.

For the fitting of the metamodel, the truncation scheme  $\mathcal{A}_{p,q}^K$  is set with  $q = 0.5$  and  $p = 10$  LARS is used. All metamodels are fitted and evaluated via UQLab (Marelli & Sudret, 2014), (Marelli et al., 2022). Once all metamodels  $\mathcal{M}_{j,PCE}^{(m)}$  are obtained, their coefficients of determination  $R^2$  are calculated on a test set of  $N_{test} = 1000$  samples.

**Table 2:** Coefficients of determination  $R^2$  of the metamodels  $\mathcal{M}_j^{(m)}$  built on the  $j$ th principal component of plot  $m$  for  $j \in \{1, 2\}$ .

$m$	1	2	3	4	5	6	7	8	9	10	11	12	13	14
$R^2$ on $\mathcal{M}_{1,PCE}^{(m)}$	1.00	0.99	0.99	0.99	0.99	0.99	0.99	1.00	0.99	0.99	1.00	0.99	0.98	0.99
$R^2$ on $\mathcal{M}_{2,PCE}^{(m)}$	NA	0.80	0.77	0.99	NA	0.97	0.82	NA	0.80	0.98	NA	0.95	0.78	0.99

The coefficients  $R^2$  calculated on the test set are reported in Table 2. The values of  $R^2$  are superior to 0.99 for all plots on the PC1. When it comes to the coefficients  $R^2$  of the metamodels built on the PC2,  $\mathcal{M}_{2,PCE}^{(m)}$ , they are slightly lower for some plots. More in particular, the parcels  $\{4, 6, 10, 12, 14\} \notin \mathcal{G}_{sat}$  have an  $R^2 > 0.95$ , whereas the parcels from  $\mathcal{G}_{sat} = \{2, 3, 7, 9, 13\}$  have lower  $R^2$  values, ranging from 0.77 for plot  $m = 3$  up to 0.82 for plot  $m = 7$ .

These lower values on  $\mathcal{M}_{2,PCE}^{(m)}$  can be explained by the choice of our methodology and the nature of the PC2. Indeed, plots belonging to group  $\mathcal{G}_{sat}$  present mostly outputs that reach a saturation point, resulting in a plateau, at some point of the simulation period. However, not all simulations of the sample have this behavior, some simulations do not reach a saturation point, as it can be seen on Figure 2 for plot  $m = 13$  (about 200 on the 3000 simulations). Calculating the principal components on such outputs, while using the  $L^2$  norm as the distance measure, results in a separation on the PC2 for the two types of behavior. Two distinct clusters are thus observed, one cluster contains the simulations reaching a plateau (lower scores on the PC2), while the other cluster contains simulations with no plateaus (scoring higher on the PC2). However, the cluster of simulations with lower scores on the PC2 has a larger cardinality (2800) than the cluster with the higher scores (200). Thus, when the PCE is evaluated on these scores, it replicates essentially the behavior of the simulations reaching saturation. Figure 4 shows the comparison between the metamodel and the PESHMELBA model outputs. The  $\mathcal{M}_{PCE}$  estimates well the behavior of lower scores, but it fails in replicating the behavior producing the simulations that do not reach saturation.

A slight increase of  $R^2$  is achieved when the values of  $p$  and  $q$  are augmented. In spite of the improvement in the  $R^2$ , the Sobol' indices calculated in both cases remain qualitatively the same. In addition, no improvement is observed in the precision of their estimates. The results for the Sobol' indices presented in Section 4.3 are listed for the metamodels built for  $p = 10$ ,  $q = 0.5$  which is a good compromise for the numerical cost.

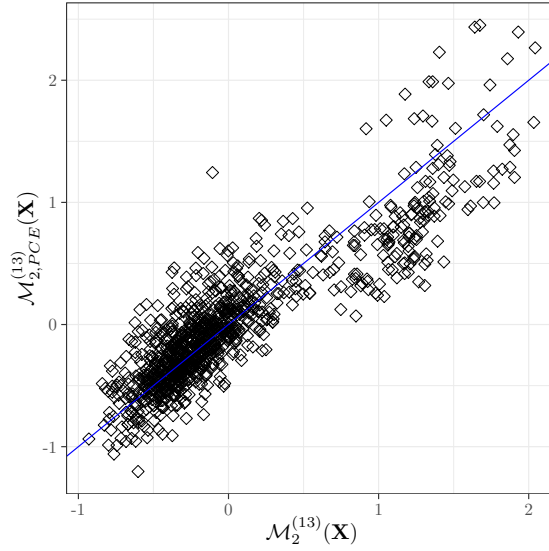


**Figure 4:** Comparison of the outputs generated by the original model  $\mathcal{M}_2^{(13)}$  versus the outputs generated by the polynomial chaos metamodel  $\mathcal{M}_{2,PCE}^{(13)}$  for the PC2 of plot  $m = 13$ . The test set is made out of  $N_{test} = 1000$  points

### 4.3 Sobol' indices

Once the metamodels are built as presented in Section 4.2, the Sobol' indices are calculated analytically via Eq. (3), for the PC1 of plots  $m \in \{1, \dots, 14\}$  in Section 4.3.1 and for the PC2 of plots  $m \in \{1, \dots, 14\} \setminus \{1, 5, 8, 11\}$  in Section 4.3.2.

#### 4.3.1 Sobol' indices on the first principal component PC1

The Sobol' indices of total order for the PC1 of each plot of the catchment are reported in Figure 5. First order Sobol' indices are nearly identical to the total order indices, meaning that the direct influence of the input parameters on the PC1 surpasses the influence through interaction with other parameters.

- *Soil type SU1 (sandy), PC1.* The top row of Figure 5 represents the total Sobol' indices of the plots of soil type SU1 ( $m \in \{1, 2, 3, 5, 11\}$ ). The largest Sobol indices correspond to parameters describing the surface soil horizon properties of the soil type SU1. More in particular, the input parameter  $\theta_{surf\_soil1}$  (resp.  $\theta_{surf\_soil1}(VFZ)$ ) accounts for more than 90% of the total output variance of the surface moisture of vineyard plots (resp. vegetative filter strips). This parameter describes the water content at saturation in a given soil, in this case the surface soil horizon of vineyard plots of soil type SU1 (resp. vegetative filter strips of soil type SU1). The second most influential input parameter,  $mn\_surf\_soil1$  (resp.  $mn\_surf\_soil1(VFZ)$ ) is a parameter governing the relation in Van Genuchten soil hydraulic property description of the surface soil horizon of the vineyard plots belonging to soil type SU1 (resp. vegetative filter strips of soil type SU1), (Van Genuchten, 1980).

- *Soil types SU2 (sandy soil on clay) and SU3 (heterogeneous sandy soil), PC1.* Total Sobol' indices of plots of soil type SU2 (resp SU3) are reported in the middle row (resp. bottom row) of Figure 5. The physical interpretation of the results is the same as for the soil type SU1. Once again, the output variability is mostly due to the variability of parameters describing the surface soil horizon properties. In particular, the input parameter  $\theta_{surf\_soil2}$  (resp.  $\theta_{surf\_soil3}, \theta_{surf\_soil2}(VFZ), \theta_{surf\_soil3}(VFZ)$ ), describing the water content at saturation in the surface soil horizon of the vineyard plots belonging to SU2 (resp. surface of the vineyard plots belonging to SU3, surface of the vegetative filter stripes belonging to SU2 and the surface of the vegetative filter stripes belonging to SU3) has the largest total Sobol' index ( $\approx 0.9$ ). The second most influential input parameter,  $mn\_surf\_soil2$  (resp.  $mn\_surf\_soil3, mn\_surf\_soil2(VFZ), mn\_surf\_soil$ ) is a parameter governing the relation in Van Genuchten soil hydraulic property description of the surface soil horizon belonging to the corresponding soil type (Van Genuchten, 1980).

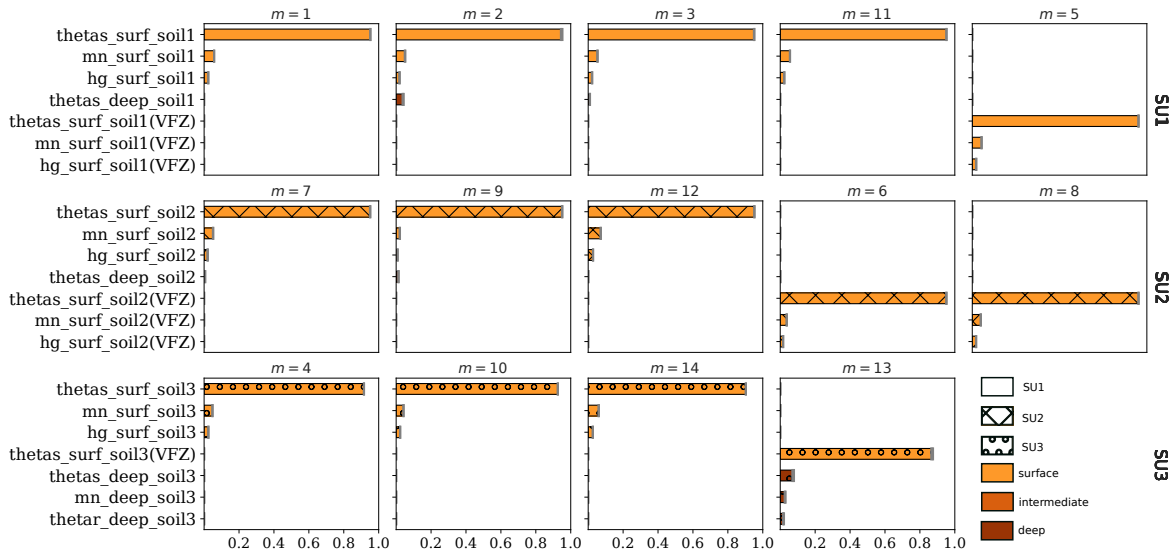


**Figure 5:** Sobol' indices of total order calculated on PC1 of each plot of the catchment  $m \in \{1, \dots, 14\}$ , with corresponding bootstrap confidence limits. Rows correspond to soil types SU1, SU2 and SU3. The top seven parameters with the highest total Sobol' index are reported for each soil type. The color and the filling of the bars represent the nature of the input parameters. The light, medium and dark brown correspond respectively to those parameters that describe the physical properties of the surface, intermediate and deep soil horizon. The different fillings of the bars correspond to those parameters that describe the soil types SU1, SU2 and SU3. The colors and fillings are in line with those from Figure 1.

We can conclude that, for a fixed plot, the variability of the PC1, interpreted in Section 4.1 as the average surface moisture over the observed time period, can be traced back to the variability of the input parameters describing the hydrodynamical properties (predominantly water content at saturation) of its surface soil horizon.

However, we find some cases which show influence of deeper soil parameters, such as  $m \in \{2, 13\}$ . Both plots  $m = 2$  and  $m = 13$  belong to group  $\mathcal{G}_{sat}$  and present plateaus in their output time series. The influence of deeper soil parameters is more prominent in PC2 and is commented in Section 4.3.2.

The Sobol' indices presented in Figure 5 were estimated with a high precision, as can be seen from the small standard deviations calculated with a bootstrap of 100 runs. This is in line with the high values of the determination coefficient  $R^2$  previously seen in Table 2.

#### 4.3.2 Sobol' indices on the second principal component PC2

For the second principal component PC2, the Sobol' indices of total order for all plots except  $\{1, 5, 8, 11\}$  are reported in Figure 6. These plots were excluded from this study as their PC2 accounts for less than 1% of the total output variance (Table 1). Two types of behavior can be observed in Figure 6. We can identify plots  $m \in \{4, 6, 10, 12, 14\} \notin \mathcal{G}_{sat}$  where surface parameters are most influential, and plots  $m \in \{2, 3, 7, 9, 13\} \in \mathcal{G}_{sat}$  where deep parameters govern the output variability.

The dependence on deep soil properties of group  $\mathcal{G}_{sat}$  communicates that the saturation of the surface moisture is not limited to the surface layers. Rather, the whole soil column under the plot is saturated, thus the surface runoff observed is due to saturation excess overland flow.

We can conclude that the variability of the contrast in surface moisture during the plateau and outside of the plateau for plots  $m \in \mathcal{G}_{sat}$  can be traced back to the variability of the input parameters describing the hydrodynamical properties of its deep soil horizon. The amplitude of the surface moisture time series for plots  $m \notin \mathcal{G}_{sat}$  is governed by the input parameters describing the hydrodynamical properties of its surface soil horizon.

The standard deviations calculated with a bootstrap of 100 runs are depicted on Figure 6 are slightly larger

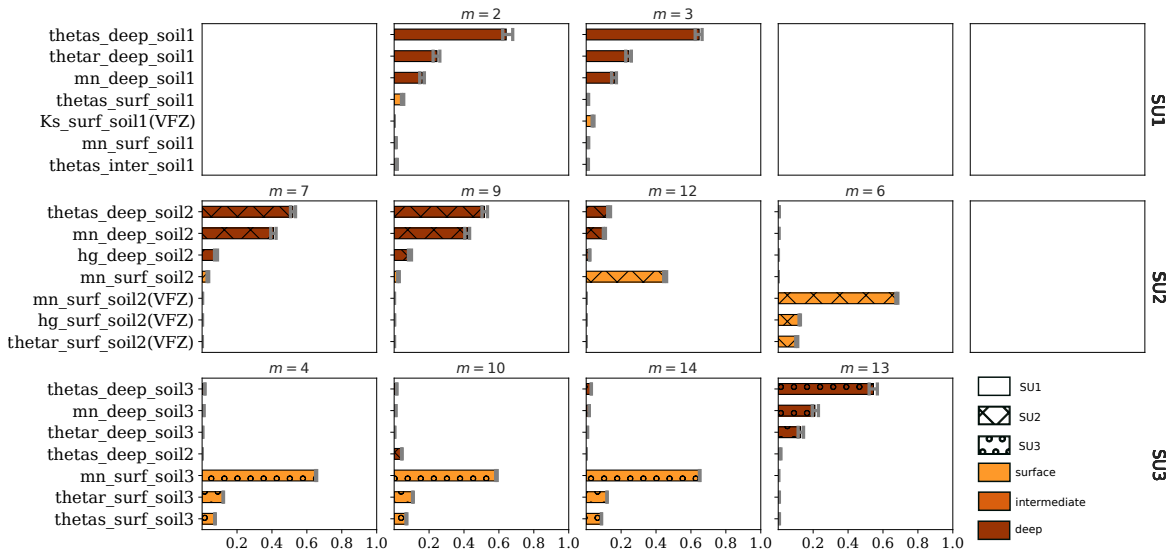


**Figure 6:** Sobol' indices of total order calculated on PC2 of plots  $m \in \{2, 3, 7, 9, 12, 6, 4, 10, 14, 13\}$ , with corresponding bootstrap confidence limits. Rows correspond to soil types SU1, SU2 and SU3. The top seven parameters with the highest total Sobol' index are reported for each soil type. The color and the filling of the bars represent the nature of the input parameters. The light, medium and dark brown correspond respectively to those parameters that describe the physical properties of the surface, intermediate and deep soil horizon. The different fillings of the bars correspond to those parameters that describe the soil types SU1, SU2 and SU3. The colors and fillings are in line with those from Figure 1.

than in Figure 5 for plots belonging to  $\mathcal{G}_{sat}$ . This is in line with what was observed previously in Table 2; the determination coefficient  $R^2$  was lower on the metamodels built on PC2, especially for plots belonging to  $\mathcal{G}_{sat}$ . Nonetheless, the precision of Sobol' indices is still satisfactory.

#### 4.3.3 Aggregation to the catchment scale

To obtain synthetic sensitivity indices of the input parameters over the whole spatio-temporal domain, the Sobol' indices on PC1 and PC2 from Sections 4.3.1 and 4.3.2 are aggregated temporally using Eq. 7 where  $j \in 1, 2$  and for plot  $m$ :  $\lambda_1 = \lambda_1^{(m)}$  and  $\lambda_2 = \lambda_2^{(m)}$ . Then, the obtained  $GSI_w^{(m)}$  sensitivity indices are aggregated spatially using Eq. 8 with  $M = 14$ ,  $\mathbb{V}ar(Y^{(m)}) = \lambda_1^{(m)} + \lambda_2^{(m)}$  and  $SI_{w,m} = GSI_w^{(m)}$ .

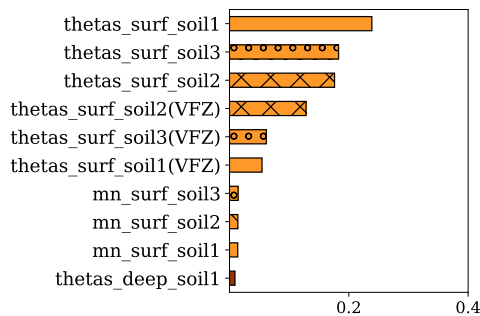


**Figure 7:** Aggregated GSI of all plots at the catchment scale. Ten input parameters with the highest GSI are reported. The color and filling of the bars represents the nature of the input parameters as in Figures 1, 5 and 6.

Spatio-temporal sensitivity indices are reported on Figure 7. They are essentially a summary of the results presented in Sections 4.3.1 and 4.3.2. As PC1 explains over 80% of the total variability of each plot (Table 1),

and as  $\theta_{surf}$  has a Sobol index superior to 0.85 (Figure 5), it comes as no surprise that by doing a weighted average (Eq. 7) and (Eq. 8), the most influential parameters are the  $\theta_{surf}$  of all soil types and vegetative filter strips, ordered by the number of plots belonging each soil type.

## 5 Conclusion

In this work, variance-based sensitivity indices are calculated for the surface moisture outputs of the PESH-MELBA model. The sensitivity indices consider both the temporal and the spatial aspect of the output. Firstly, the most influential input parameters on the output dynamics are obtained for the first two functional principal components of every plot on the catchment. Then, these sensitivity indices are aggregated temporally and spatially, enabling a synthetic view of the most influential parameters on the whole spatio-temporal domain. Notably, the surface hydrodynamic parameters have a predominant influence on the catchment's surface moisture. In particular, the input parameters describing the water content at saturation of all soil types constituting the catchment account for more than 80% of the total output variability.

This synthetic view provides a summary of the most influential parameters at the catchment scale, however in order to understand local contributions to the dynamics, the Sobol' indices calculated on the principal components are more informative. Thus, the average surface moisture of the period is governed by the surface soil hydrodynamic properties. Furthermore, the contrast between the surface moisture during saturated periods and unsaturated periods is influenced by deep soil hydrodynamic properties. The dependence on deep soil properties implies that the saturation in water is not limited to the surface layers. Rather, the whole soil column under the plot is saturated. Hence, the surface runoff observed on these plots is due to saturation excess overland flow

The use of PCE metamodells for the calculation of Sobol' indices lowers significantly the number of PESH-MELBA model simulations needed. Indeed, only 3000 model simulations are used to calculate all sensitivity indices with high precision.

Further research could focus on the application of cluster based approaches, such as in Roux et al. (2021), thus distinguishing the inter and intra variability of the simulations that reach surface moisture saturation and those who don't. Additionally, other sensitivity indices, such as the HSIC could be adapted to spatio-temporal outputs and compared to the indices obtained in this work.

## Declaration of competing interest

The authors declare that they have no known competing financial interest or personal relationship that could have appeared to influence the work reported in this paper.

## Acknowledgements

We thank Xujia Zhu, Matieyendou Lamboni and Céline Helbert for their insights which have enriched this work.

## References

- Antoniadis, A., Lambert-Lacroix, S., & Poggi, J.-M. (2021). Random forests for global sensitivity analysis: A selective review. *Reliability Engineering & System Safety*, 206:107312. <https://doi.org/10.1016/j.res.2020.107312>.
- Blatman, G. & Sudret, B. (2011). Adaptive sparse polynomial chaos expansion based on least angle regression. *Journal of Computational Physics*, 230(6):2345–2367. <https://doi.org/10.1016/j.jcp.2010.12.021>.
- Buis, S., Piacentini, A., Déclat, D., & the PALM Group (2006). PALM: a computational framework for assembling high-performance computing applications. *Concurrency and Computation: Practice and Experience*, 18(2):231–245. <https://doi.org/10.1002/cpe.914>.

- Da Veiga, S. (2015). Global sensitivity analysis with dependence measures. *Journal of Statistical Computation and Simulation*, 85(7):1283–1305. <https://doi.org/10.1080/00949655.2014.945932>.
- De Lozzo, M. & Marrel, A. (2017). Sensitivity analysis with dependence and variance-based measures for spatio-temporal numerical simulators. *Stochastic Environmental Research and Risk Assessment*, 31(6):1437–1453. <https://doi.org/10.1007/s00477-016-1245-3>.
- Dubreuil, S., Berveiller, M., Petitjean, F., & Salaün, M. (2014). Construction of bootstrap confidence intervals on sensitivity indices computed by polynomial chaos expansion. *Reliability Engineering & System Safety*, 121:263–275. <https://doi.org/10.1016/j.res.2013.09.011>.
- Fajraoui, N., Ramasomanana, F., Younes, A., Mara, T. A., Ackerer, P., & Guadagnini, A. (2011). Use of global sensitivity analysis and polynomial chaos expansion for interpretation of nonreactive transport experiments in laboratory-scale porous media. *Water Resources Research*, 47(2). <https://doi.org/10.1029/2010WR009639>.
- Ferrer Savall, J., Franqueville, D., Barbillon, P., Benhamou, C., Durand, P., Taupin, M.-L., Monod, H., & Drouet, J.-L. (2019). Sensitivity analysis of spatio-temporal models describing nitrogen transfers, transformations and losses at the landscape scale. *Environmental Modelling & Software*, 111:356–367. <https://doi.org/10.1016/j.envsoft.2018.09.010>.
- Gamboa, F., Janon, A., Klein, T., & Lagnoux, A. (2014). Sensitivity analysis for multidimensional and functional outputs. *Electronic Journal of Statistics*, 8(1). <https://doi.org/10.1214/14-EJS895>.
- Lamboni, M., Monod, H., & Makowski, D. (2011). Multivariate sensitivity analysis to measure global contribution of input factors in dynamic models. *Reliability Engineering & System Safety*, 96(4):450–459. <https://doi.org/10.1016/j.res.2010.12.002>.
- Le Gratiet, L., Marelli, S., & Sudret, B. (2015). Metamodel-based sensitivity analysis: Polynomial chaos expansions and Gaussian processes. pages 1–37. arXiv:1606.04273.
- Marelli, S., Lüthen, N., & Sudret, B. (2022). UQLab user manual – Polynomial chaos expansions. Technical report, Chair of Risk, Safety and Uncertainty Quantification, ETH Zurich, Switzerland. Report UQLab-V2.0-104.
- Marelli, S. & Sudret, B. (2014). UQLab: A Framework for Uncertainty Quantification in Matlab. In *Vulnerability, Uncertainty, and Risk*, pages 2554–2563, Liverpool, UK. American Society of Civil Engineers. <https://doi.org/10.1061/9780784413609.257>.
- Marrel, A., Perot, N., & Mottet, C. (2015). Development of a surrogate model and sensitivity analysis for spatio-temporal numerical simulators. *Stochastic Environmental Research and Risk Assessment*, 29(3):959–974. <https://doi.org/10.1007/s00477-014-0927-y>.
- Morris, M. D. (1991). Factorial Sampling Plans for Preliminary Computational Experiments. *Technometrics*, 33(2):161–174. <https://doi.org/10.1080/00401706.1991.10484804>.
- Perrin, T., Roustant, O., Rohmer, J., Alata, O., Naulin, J., Idier, D., Pedreros, R., Moncoulon, D., & Tinard, P. (2021). Functional principal component analysis for global sensitivity analysis of model with spatial output. *Reliability Engineering & System Safety*, 211:107522. <https://doi.org/10.1016/j.res.2021.107522>.
- Ramsay, J. O. & Silverman, B. W. (2005). *Functional data analysis*. Springer series in statistics. Springer, New York, 2nd edition.
- Ross, P. J. (2003). Modeling Soil Water and Solute Transport—Fast, Simplified Numerical Solutions. *Agronomy Journal*, 95(6):1352–1361. <https://doi.org/10.2134/agronj2003.1352>.
- Roux, S., Buis, S., Lafolie, F., & Lamboni, M. (2021). Cluster-based GSA: Global sensitivity analysis of models with temporal or spatial outputs using clustering. *Environmental Modelling & Software*, 140:105046. <https://doi.org/10.1016/j.envsoft.2021.105046>.
- Rouzies, E., Lauvernet, C., Barachet, C., Morel, T., Branger, F., Braud, I., & Carlier, N. (2019). From agricultural catchment to management scenarios: A modular tool to assess effects of landscape features on water and pesticide behavior. *Science of The Total Environment*, 671:1144–1160. <https://doi.org/10.1016/j.scitotenv.2019.03.060>.
- Rouzies, E., Lauvernet, C., Sudret, B., & Vidard, A. (2021). How to perform global sensitivity analysis of a catchment-scale, distributed pesticide transfer model? application to the peshmelba model. *Geoscientific Model Development*

- Discussions*, 2021:1–44. <https://doi.org/10.5194/gmd-2021-425>.
- Saltelli, A., Ratto, M., Andres, T., Campolongo, F., Cariboni, J., Gatelli, D., Saisana, M., & Tarantola, S. (2008). *Global sensitivity analysis: the primer*. John Wiley & Sons. <https://dx.doi.org/10.1002/9780470725184>.
- Sobol', I. (2001). Global sensitivity indices for nonlinear mathematical models and their Monte Carlo estimates. *Mathematics and Computers in Simulation*, 55(1-3):271–280. [https://doi.org/10.1016/S0378-4754\(00\)00270-6](https://doi.org/10.1016/S0378-4754(00)00270-6).
- Sudret, B. (2008). Global sensitivity analysis using polynomial chaos expansions. *Reliability Engineering & System Safety*, 93(7):964–979. <https://doi.org/10.1016/j.ress.2007.04.002>.
- Van Genuchten, M. T. (1980). A Closed-form Equation for Predicting the Hydraulic Conductivity of Unsaturated Soils. *Soil Science Society of America Journal*, 44(5):892–898. <https://doi.org/10.2136/sssaj1980.03615995004400050002x>.
- Xiao, H. & Li, L. (2016). Discussion of paper by Matieyendou Lamboni, Hervé Monod, David Makowski “Multivariate sensitivity analysis to measure global contribution of input factors in dynamic models”, *Reliab. Eng. Syst. Saf.* 99 (2011) 450–459. *Reliability Engineering & System Safety*, 147:194–195. <https://doi.org/10.1016/j.ress.2015.10.015>.
- Xu, L., Lu, Z., & Xiao, S. (2019). Generalized sensitivity indices based on vector projection for multivariate output. *Applied Mathematical Modelling*, 66:592–610. <https://doi.org/10.1016/j.apm.2018.10.009>.

**Table 3:** List of PESHMELBA model parameters selected for the sensitivity analysis. The suffixes surf, interm and deep specify the soil horizon, while suffixes soil1, soil2 and soil3 specify the soil type (SU1, SU2, SU3). The suffix (VFZ) is present for parameters of vegetative buffer strips. Gaussian, lognormal and uniform distributions are listed as  $\mathcal{N}(\mu, \sigma)$ ,  $\mathcal{LN}(\mu, \sigma)$  and  $U(a, b)$ . The parameter thetar is bounded to positive values only.

Name	Definition	Unit	Distribution	
thetas_surf_soil1	water content at saturation	$[L^3 L^{-3}]$	$\mathcal{N}(0.3375, 0.0338)$	
thetas_interm_soil1		$[L^3 L^{-3}]$	$\mathcal{N}(0.3362, 0.0336)$	
thetas_deep_soil1		$[L^3 L^{-3}]$	$\mathcal{N}(0.2844, 0.0284)$	
thetas_surf_soil2		$[L^3 L^{-3}]$	$\mathcal{N}(0.3375, 0.0338)$	
thetas_interm_soil2		$[L^3 L^{-3}]$	$\mathcal{N}(0.3537, 0.0354)$	
thetas_deep_soil2		$[L^3 L^{-3}]$	$\mathcal{N}(0.4162, 0.0416)$	
thetas_surf_soil3		$[L^3 L^{-3}]$	$\mathcal{N}(0.3375, 0.0338)$	
thetas_interm_soil3		$[L^3 L^{-3}]$	$\mathcal{N}(0.3322, 0.0332)$	
thetas_deep_soil3		$[L^3 L^{-3}]$	$\mathcal{N}(0.316, 0.0316)$	
thetas_surf_soil1(VFZ)		$[L^3 L^{-3}]$	$\mathcal{N}(0.3375, 0.0338)$	
thetas_surf_soil2(VFZ)		$[L^3 L^{-3}]$	$\mathcal{N}(0.3375, 0.0338)$	
thetas_surf_soil3(VFZ)		$[L^3 L^{-3}]$	$\mathcal{N}(0.3375, 0.0338)$	
thetar_surf_soil1		residual water content	$[L^3 L^{-3}]$	$\mathcal{N}(0.0372, 0.0093)$
thetar_deep_soil1	$[L^3 L^{-3}]$		$\mathcal{N}(0.0661, 0.0165)$	
thetar_surf_soil2	$[L^3 L^{-3}]$		$\mathcal{N}(0.0372, 0.0093)$	
thetar_interm_soil2	$[L^3 L^{-3}]$		$\mathcal{N}(0, 0.0093)$	
thetar_deep_soil2	$[L^3 L^{-3}]$		$\mathcal{N}(0, 0.0093)$	
thetar_surf_soil3	$[L^3 L^{-3}]$		$\mathcal{N}(0.0372, 0.0093)$	
thetar_deep_soil3	$[L^3 L^{-3}]$		$\mathcal{N}(0.0612, 0.0153)$	
thetar_surf_soil1(VFZ)	$[L^3 L^{-3}]$		$\mathcal{N}(0.0372, 0.0093)$	
thetar_surf_soil2(VFZ)	$[L^3 L^{-3}]$		$\mathcal{N}(0.0372, 0.0093)$	
hg_surf_soil1	Van Genuchten water retention curve parameter		[-]	$\mathcal{N}(-9.69, 0.969)$
hg_surf_soil2			[-]	$\mathcal{N}(-9.69, 0.969)$
hg_deep_soil2			[-]	$\mathcal{N}(-30.18, 3.018)$
hg_surf_soil3			[-]	$\mathcal{N}(-9.69, 0.969)$
hg_surf_soil1(VFZ)		[-]	$\mathcal{N}(-9.69, 0.969)$	
hg_surf_soil2(VFZ)		[-]	$\mathcal{N}(-9.69, 0.969)$	
hg_surf_soil3(VFZ)		[-]	$\mathcal{N}(-9.69, 0.969)$	
mn_surf_soil1		Van Genuchten water retention curve parameter	[-]	$\mathcal{N}(0.2685, 0.0268)$
mn_deep_soil1			[-]	$\mathcal{N}(0.2274, 0.0227)$
mn_surf_soil2	[-]		$\mathcal{N}(0.2685, 0.0268)$	
mn_interm_soil2	[-]		$\mathcal{N}(0.1289, 0.0129)$	
mn_deep_soil2	[-]		$\mathcal{N}(0.1, 0.01)$	
mn_surf_soil3	[-]		$\mathcal{N}(0.2685, 0.0268)$	
mn_deep_soil3	[-]		$\mathcal{N}(0.1791, 0.0179)$	
mn_surf_soil1(VFZ)	[-]		$\mathcal{N}(0.2685, 0.0268)$	
mn_surf_soil2(VFZ)	[-]		$\mathcal{N}(0.2685, 0.0268)$	
mn_surf_soil3(VFZ)	[-]	$\mathcal{N}(0.2685, 0.0268)$		
Ks_surf_soil2	hydraulic conductivity at total saturation	$[cm/h]$	$\mathcal{LN}(2.6291, 0.198)$	
Ks_interm_soil2		$[cm/h]$	$\mathcal{LN}(2.0292, 0.198)$	
Ks_interm_soil2		$[cm/h]$	$\mathcal{LN}(1.2206, 0.198)$	
Ks_deep_soil2		$[cm/h]$	$\mathcal{LN}(0.3391, 0.198)$	
Ks_interm_soil3		$[cm/h]$	$\mathcal{LN}(2.3762, 0.198)$	
Ks_surf_soil1(VFZ)		$[cm/h]$	$\mathcal{LN}(2.6884, 0.198)$	
Ks_surf_soil2(VFZ)		$[cm/h]$	$\mathcal{LN}(2.6884, 0.198)$	
Ks_surf_soil3(VFZ)		$[cm/h]$	$\mathcal{LN}(2.6884, 0.198)$	
Kx_surf_soil2		hydraulic conductivity at soil matrix saturation	$[cm/h]$	$\mathcal{LN}(-2.2926, 0.198)$
Kx_interm_soil2	$[cm/h]$		$\mathcal{LN}(-2.833, 0.198)$	
veget_LAI <sub>max_1</sub>	maximal Leaf Area Index	[-]	$U(2, 3)$	
plot_hpond	maximal ponding height of the plots	$[cm]$	$U(0.8, 1.2)$	
river_di	distance between the riverbed and the aquifer	$[cm]$	$U(120, 180)$	
river_ks	hydraulic conductivity of the riverbed at saturation	$[cm/h]$	$\mathcal{LN}(2.1268, 0.198)$	